A Two-step Displacement Correction Algorithm for Registration of Lidar Point Clouds and Aerial Images without Orientation Parameters

Huayi Wu, Yong Li, Jonathan Li, and Jianya Gong

Abstract

This paper presents a novel linear registration algorithm for lidar point clouds and aerial images without orientation parameters. First, preprocessing is conducted to classify the lidar point clouds into ground points, building points, and aboveground, non-building points. After preprocessing, the algorithm consists of two sequential steps, i.e., Tilt Displacement Correction and Height Displacement Correction. As the kernel of the proposed registration algorithm, the mathematical model for Height Displacement Correction is a set of linear formulas analytically deduced from the rigorous geometric function of a single image. The proposed registration algorithm does not require any orientation parameters for the image, which greatly lowers the requirements for image acquisition. Due to the model's linearity, the proposed algorithm is computationally efficient. Our experimental results demonstrate that the proposed algorithm can register aerial images without orientation parameters at the same accuracy level of space resection based on collinear equations. This result fulfills the requirement for the fusion of lidar range data and aerial images in most large-scale urban modeling applications.

Introduction

Driven by technological developments, the last decade witnessed fast-growing demands for three-dimensional (3D) city models. Both topographic Light Detection And Ranging (lidar) point cloud data and high-resolution aerial imagery data provide powerful support for creating 3D city models with highly detailed information. With the capability of acquiring discrete and densely distributed 3D point clouds, lidar is widely used to produce digital surface models and digital elevation models (DSMs/DEMs) and to extract geometric features of objects (e.g., buildings). However, lidar acquires 3D points by discontinuous laser pulses. With lidar, very few points on building edges can be exactly hit by laser pulses. Therefore, the horizontal accuracy of the edges detected from lidar point clouds is generally not satisfied. High-resolution aerial imagery has higher horizontal accuracy for edge detection and rich spectral and texture information, which can improve the corresponding lidar data segmentation and classification. Aerial imagery can also act as textures on surfaces of 3D building models to enhance the visual effects in virtual environments. Many sophisticated algorithms have been developed for deriving 3D information from aerial imagery. However, automatic matching in photogrammetry is still a complicated and unreliable procedure, especially when dealing with large-scale aerial imagery of urban areas with tall and densely distributed buildings. Meanwhile, the spectral information in such imagery is often too rich to segment objects when image data is the only available data source. Thus, the fusion of lidar point clouds and aerial imagery is considered as one of the most promising approaches for creating 3D city models (Rottensteiner and Jansa, 2002; Fujii and Arikawa, 2002; McIntosh and Krupnik, 2002; Rottensteiner, 2003; Zhou *et al.* 2004; Rottensteiner *et al.* 2005; Chen *et al.* 2006; You and Zhang, 2006; Demir *et al.* 2008; Dorninger and Pfeifer, 2008; Poullis and You, 2009), and detecting trees (Secord and Zakhor, 2007; Dalponte *et al.* 2008), as well as detection of the building changes in urban areas (Murakami *et al.* 1999). Brenner (2005) reviews a number of automatic and semi-automatic building reconstruction methods, and concluded that combining aerial photogrammetry and laser scanning is the superior way to increase automation and obtain very accurate results. As the first and most important step, developing a fast and reliable registration algorithm for these two data sources is critical to this fusion approach.

Due to their distinct natures, the registration of lidar point cloud data and aerial imagery is challenging, especially when the image is not rectified. Collinearity and coplanarity are the most intuitive constraints for registration. Deng *et al.* (2008) proposed a registration algorithm by matching the straight-line pairs detected from lidar point clouds and optical images using generalized point photogrammetry. In generalized point photogrammetry, a collinear equation is applied to match linear features.

Huayi Wu, Yong Li, and Jianya Gong are with the State Key Laboratory of Surveying, Mapping and Remote Sensing, Wuhan University, 129 Luoyu Road, Wuhan, 430079, China, (wuhuayi@lmars.whu.edu.cn)

Jonathan Li is with the Department of Geography and Environmental Management, University of Waterloo, 200 University Avenue West, Waterloo, Ontario, Canada N2L 3G1.

Photogrammetric Engineering & Remote Sensing
Vol. 76, No. 10, October 2010, pp. 1135–1145.

0099-1112/10/7610–1135/$3.00/0

Habib *et al.* (2005a) incorporated the straight line features derived from lidar data and images in photogrammetric triangulation. The photogrammetric dataset is aligned to the lidar reference frame through direct incorporation of lidar lines as the source of control in the photogrammetric bundle adjustment procedure. A similarity measure is designed to mathematically ensure that the lidar lines projected onto the image space coincide with the corresponding image lines. The transformation and similarity measure are both implemented simultaneously in a coplanarity condition. Habib *et al.* (2005b) introduced another approach which starts by manipulating the photogrammetric imagery to produce a 3D model, including a set of linear features along object space discontinuities, relative to an arbitrarily chosen coordinate system. Afterwards, conjugate photogrammetric and lidar straight line features are used to establish the transformation between the arbitrarily chosen photogrammetric coordinate system and the lidar reference frame. Habib *et al.* (2006) aligned lidar and photogrammetric data relative to a common reference frame using linear and areal primitives, which are based on a modified coplanarity constraint. Liu *et al.* (2007) utilized lidar intensity images to collect highly accurate coordinates of ground control points (GCPs) and generate a high quality DEM from lidar data for orthorectification by an aerial triangulation calculation. However, all these methods require Interior Orientation Parameters (IOPs). The camera must be strictly calibrated before acquiring images. It is important to note that the transformation functions in the above algorithms are nonlinear requiring linearization preprocessing. To solve the transformation functions, an iterative algorithm is adopted so as to approach the real values. Accuracy and convergence depend strongly on the initial values.

With the significant improvement of non-metric camera performance and the advent of new remote sensing platforms such as the Unmanned Aerial Vehicle (UAV), a very attractive option is to acquire images by non-metric cameras. However, fiducial marks are not provided with non-metric cameras to get IOPs. Many free and high quality images are easily accessed in the Internet, but they also usually do not have IOPs and Exterior Orientation Parameters (EOPs). Without IOPs, it is difficult to transform the image from the pixel coordinate system to an image space coordinate system. Further without EOPs, it is difficult to offer relatively precise initial values for the iterative calculation. Some researchers have tried to use a non-metric, small format, and low cost digital camera to obtain aerial images (Delara *et al.* 2004). In their approaches, the pixel is utilized as the unit of measurement for photogrammetric observations and the determination of interior orientation parameters. The bundle block adjustment is performed by using both lidar intensity image and aerial images. These studies revealed that the utilization of the pixel as a unit in the image system is consistent and efficient. Zhang and Zhang (2004) computed image orientation parameters from vanishing points for modeling with a single image. Hu *et al.* (2006) studied the possibility of using aerial images simply downloaded from the Internet, without any orientation information. In their studies, the camera's orientation parameters are estimated by three vanishing points. The rectified image generated by the recovered camera hinges on the assumption that the difference of buildings' depth can be ignored. An affine model is used to register the rectified aerial image to the 2D range image generated from lidar data by manually selecting matching points. However, in order to obtain the camera's orientation parameters, the vanishing points of three mutually orthogonal directions are necessary, which is not an easy task for all aerial images.

The vanishing point of the vertical direction is referred to as the photo's nadir point in photogrammetry. A large number of vertical lines can be identified in urban areas, for example, the intersections of building walls. Thus, it is feasible to make use of these vertical lines in urban areas to acquire the nadir point. Zhang *et al.* (2007) carried out the absolute orientation of aerial imagery over urban areas combining with vertical lines according to the vanishing point theory. Zhang *et al.* (2007 and 2008) established a mathematical model for vertical lines and linear features supported aerial triangulation by vanishing point theory.

The transformation functions used in the traditional photogrammetry are based on the space resection model described by collinear equations. It is a physical sensor model whose parameters are physically meaningful and rigorous. Collinear equations are nonlinear and known oriented parameters are usually required for solving these equations by iteration. At the very least, the initial values of the orientation parameters should be provided for iteration. The success and the speed of convergence depend heavily on the quality of these initial values. In practice, the initial values are often unknown or not precise enough for a converging solution (Jiang *et al.*, 2007).

To avoid those problems of the rigorous model above, another type of transformation functions, generalized sensor models, were developed. They directly use general parametric functions to approximate the relationship between object and image pixels. Therefore, they are non-physical sensor models and do not reflect the imaging process. Typical generalized models include the polynomial model and the Rational Functional Model (RFM). The one-order RFM is identical to the Direct Linear Transform Model (DLT) as shown in Equations 1:

$$x = \frac{a_1X + a_2Y + a_3Z + a_4}{c_1X + c_2Y + c_3Z + 1}$$
$$y = \frac{b_1X + b_2Y + b_3Z + b_4}{c_1X + c_2Y + c_3Z + 1} \quad (1)$$

In the DLT model, these parameters (coefficients) do not have physical meanings, and orientation parameters are not required to solve these models. Known orientation parameters also do not contribute to improve the solving of these models. Tao and Hu (2001) studied RFM for image rectification and proposed a least-squares solution to calculate these Rational Function Coefficients (RFCs). Abedini *et al.* (2008) extract distinctive features from lidar intensity data and aerial images by the Scale Invariant Feature Transform (SIFT), then use the quadratic polynomial transformation for registration. However, the quadratic polynomial transformation only works well in the areas with slight topographic relief.

This paper presents a novel linear registration algorithm, Two-step Displacement Correction, for lidar point clouds and aerial image without orientation parameters. The algorithm is featured by a combination of two sequential displacement corrections, i.e., Tilt Displacement Correction and Height Displacement Correction. Both the two displacement corrections have explicit physical meanings. The core algorithm is linear and iteration is not necessary. The following section outlines the main steps and principles of this algorithm. The mathematical model of the Height Displacement Correction, the kernel of this method, is deduced in detail in an independent section. The last two sections describe our experimental results, discussions, and conclusions.

Methodology

The purpose of registration is to create functional spatial relations between laser footprints and image pixels. After registration, point clouds are projected on the image space so that every lidar point has spectral information in addition to its 3D coordinates, thereby improving feature extraction and texture mapping. In this paper, the lidar dataset is assumed to be geometrically true, providing both high quality control points and a digital surface model (DSM) for registration.

Other than creating direct functional spatial relations between laser footprints and image pixels, our research focuses on registration from an indirect viewpoint, i.e., image displacement. If the amount and the direction of the displacement of each lidar point are calculated, the registration can be carried out equivalently. We break down the image displacement into two sequential displacements, i.e., tilt displacement and height displacement. The registration method proposed in this paper, Two-step Displacement Correction, is designed to correct these two displacements separately and sequentially after preprocessing. The workflow of this algorithm is shown in Figure 1.

During preprocessing, lidar point clouds are classified into three categories, i.e., ground points, building points, and non-building points. This preprocessing helps the following two displacement correction steps to select the required control points for registration. Many algorithms are available for this preprocessing. In our experiments, the ground points and aboveground points are separated by a filter based on morphological gradient (Li and Wu, 2008a), while the buildings and non-building points are distinguished by a region growing algorithm based on mathematical morphology (Li and Wu, 2008b).

After the above preprocessing, the two displacement correction steps of the proposed algorithms are:

Step 1: Tilt Displacement Correction

Tilt displacement can be recognized as the displacement caused by the non-parallelity of the image plane and the datum plane in the object space. This step creates a functional relationship to map the datum plane to the image plane. It consists of sub-steps.

- Sub-step 1.1: Define a datum plane in object space.
- Sub-step 1.2: Find control points in datum plane and their correspond coordinates on the image plane. Though lidar points are densely distributed, it is not easy to define a datum that has obvious control points. To avoid this problem, Step 1.1 and Step 1.2 can be mixed. First, find candidate control points on the ground. Then from these candidate control points, select a subset that has the smallest height difference. Finally, use the average height of the points in this subset to define the datum plane. The points in this subset are the control points for tilt displacement correction.

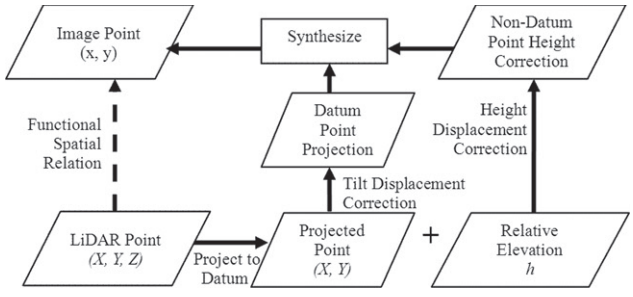

Figure 1. The Workflow of the Two-step Displacement Correction Algorithm.

- Sub-step 1.3: For these control points, project them to the datum plane, i.e., use their X and Y coordinates and omit their Z coordinates.
- Sub-step 1.4: Create tilt displacement correction function to map from the datum plane to the image plane. Perspective transformation, linear transformation, or quadratic polynomial transformation can be used to model this mapping. A least-square solution is usually applied to retrieve these coefficients. Through this mapping function, each lidar point A(X, Y, Z) can be projected to the datum, i.e., A_0(X, Y), and find its mapping pixel in image space with tilt displacement corrected, say a_0.

Step 2: Height Displacement Correction

This correction is to remove the displacement caused by the perspective geometry of the camera and the height difference of each lidar point relative to the datum plane. Height displacement radiates outward from the photo nadir point at which a vertical line through the perspective center of the camera lens intersects the image plane. This correction includes four sub-steps.

- Sub-step 2.1: Find the nadir point. There are plenty of perpendicular lines available in urban areas such as intersections of building walls. The intersection of these perpendicular lines in the image space is exactly the photo nadir point. So the photo nadir point can be determined by intersecting these perpendicular lines on the image.
- Sub-step 2.2: Create a polar coordinate system originated at the nadir point for determination of the amount and direction of height displacement.
- Sub-step 2.3: Given a lidar point A(X, Y, Z), calculate its height displacement on the image plane a_0, the pixel obtained on Sub-step 1.4. A mathematical model of this height displacement correction, including the distance and the direction, is deduced in the next section.
- Sub-step 2.4: Synthesize the distance and directional displacements to obtain the final registered point on the image plane for each lidar point.

Mathematical Model of Height Displacement Correction

The geometric model of an image is illustrated in Figure 2 where S is the perspective projection center of this image. The datum is a horizontal plane whose height is the average of the ground control points selected for Tilt

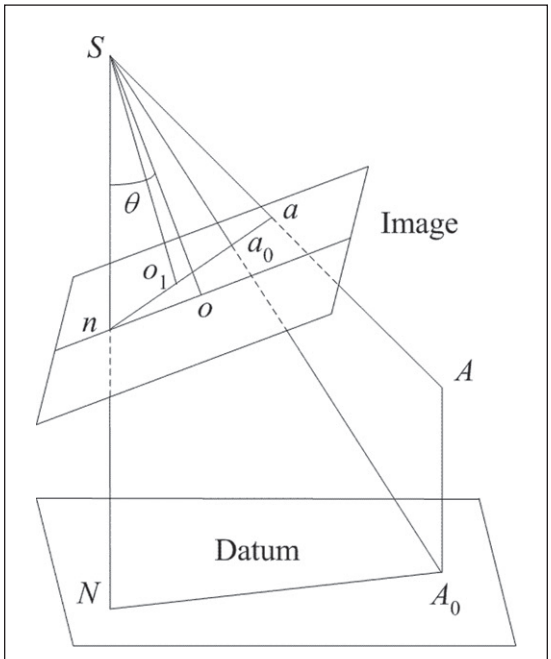

Figure 2. Geometric model of an image.

Displacement Correction. N is the ground nadir point where the perpendicular line passing through S intersects the datum plane. A is an arbitrary lidar point. A_0 is the perpendicular projection of A on the datum plane, and n is the photo nadir point where the perpendicular line passing through S intersects the image plane. The location of n is retrieved by intersecting perpendicular lines on the image, a is the corresponding image point of A, and a_0 is the corresponding image point of A_0 after Tilt Displacement Correction. The principal point of the image is o, the normal projection of S on the image plane, and o_1 is the perpendicular foot where the line na and its normal So_1 intersect. θ is the angle between the image plane and the datum plane.

In order to obtain a, the true location of A projected on the image plane, the height displacement, a-a_0, should be calculated. Figure 3 shows the geometric relationship of these entities on the perpendicular plane of SN and AA_0.

In order to calculate a-a_0, some auxiliary lines are appended in Figure 3. A_0A_1 is a parallel line of na. Point A_1 is the intersection of line A_0A_1 and the extension of line SA. o_2 is the intersection of line NA_0 and the extension of line So_1. o_3 is the intersection of line A_0A_1 and the extension of line So_2. S_1 is the intersection of line A_0A_1 and the extension of line SN. α is the angle between line Sn and line So_1. β is the angle between line So_1 and Sa_0. According to parallel condition, Equation 2 holds:

$$\frac{\delta h}{r} = \frac{A_1A_0}{A_1S_1} = \frac{h}{SS_1} \tag{2}$$

where $\delta h = aa_0$, $r = na$, and $h = AA_0$.

Equation 2 builds a bridge between object space and image space. The variables on the left side of Equation 2 can be determined in image space using pixel unit, and the variables on the right side of Equation 2 can be determined in object space using of meters. The units of both sides of the equation need not be uniform as long as both ratios are equal. The following task is to replace variables in Equation 2 by constants or variables measurable in the image space or the object space.

Equation 3 is reformatted from Equation 2:

$$\delta h = \frac{hr}{SS_1} = \frac{hr\cos\alpha}{H_1} \tag{3}$$

where $H_1 = So_3$.

From Figure 3, we can also derive Equation 4:

$$SA_0 = \frac{H}{\cos(\alpha+\beta)} = \frac{H_1}{\cos\beta} \tag{4}$$

where $H = SN$.

Equation 4 can be further reformatted to Equation 5:

$$H_1 = \frac{H\cos\beta}{\cos(\alpha+\beta)}. \tag{5}$$

By substituting Equation 5 into Equation 3, we can obtain:

$$\delta h = \frac{hr\cos\alpha\cos(\alpha+\beta)}{H\cos\beta} = \frac{hr}{H}(\cos^2\alpha - \cos\alpha\sin\alpha tg\beta). \tag{6}$$

And $tg\beta$ can be represented as Equation 7:

$$tg\beta = \frac{a_0o_1}{f_1} = \frac{na_0 - no_1}{f_1} = \frac{r_0 - f_1tg\alpha}{f_1} \tag{7}$$

where $r_0 = na_0$, $f_1 = So_1$.

Equation 8 is derived from Equations 6 and 7:

$$\delta h = \frac{hr}{H}(1 - \frac{r_0}{f_1}\sin\alpha\cos\alpha) \tag{8}$$

Considering Equation 8, only α and f_1 are not measurable or constant for a single image and must be reformatted by other variables or constants. Figure 4 is a part of the

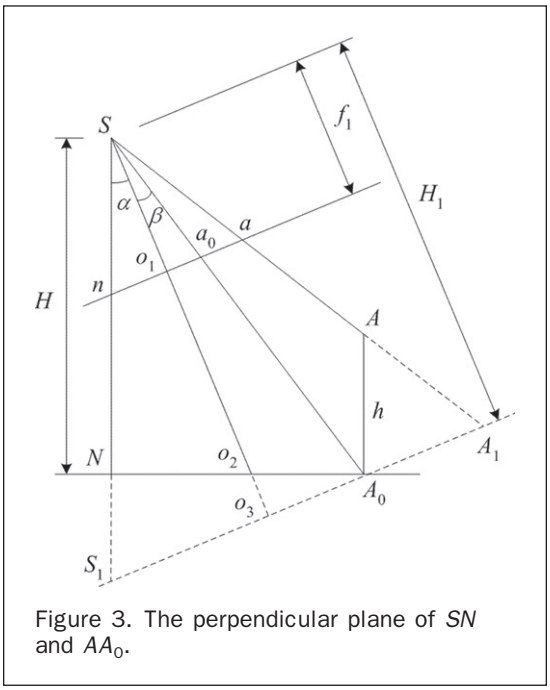

Figure 3. The perpendicular plane of SN and AA_0.

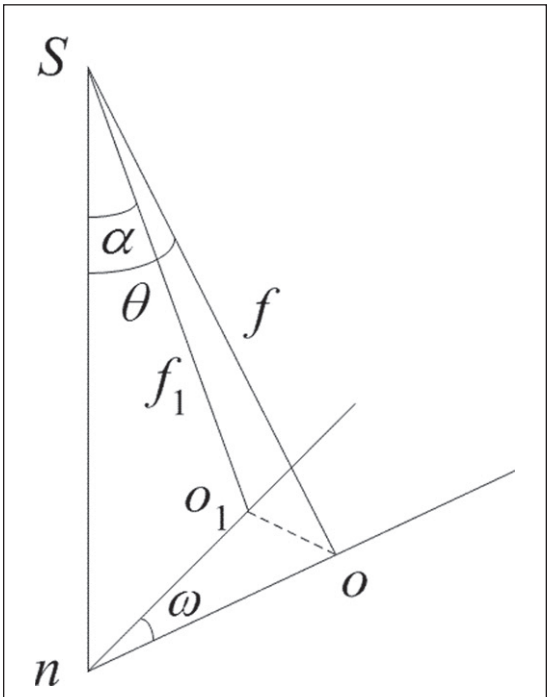

Figure 4. Sub-graph of Figure 2.

geometric model in Figure 2 highlighting the local geometry. f is the distance of So, namely principal distance. ω is the angle between no and no_1. Equations 9 can be derived from Figure 4:

$$\cos\omega = \frac{\sin\alpha}{\sin\theta}$$
$$\frac{f}{\cos\theta} = \frac{f_1}{\cos\alpha}. \tag{9}$$

Equations 9 can be rearranged into Equations 10:

$$\sin\alpha = \cos\omega\sin\theta$$
$$f_1 = f\frac{\cos\alpha}{\cos\theta}. \tag{10}$$

α and f_1 in Equation 8 can be replaced by Equations 10, which leads to Equation 11:

$$\delta h = \frac{hr}{H}(1 - r_0\cos\omega\frac{\sin\theta\cos\theta}{f}). \tag{11}$$

In Equation 11, only ω cannot be determined because the location of principal point o is unknown. A planar polar coordinate system is created around n in image space shown as Figure 5. The polar axis is from point n to horizontal right. φ_0 is the polar angle of o which is anticlockwise from polar axis. φ is the polar angle of o_1 which is counterclockwise from polar axis. Then ω can be represented as Equation 12:

$$\omega = \varphi - \varphi_0. \tag{12}$$

By substituting Equation 12 into Equation 11, we can obtain the following linear function (Equation 13):

$$l = c_0 + c_1x + c_2y \tag{13}$$

where $c_0 = \frac{1}{H}$, $c_1 = -\frac{\cos\varphi_0\sin\theta\cos\theta}{fH}$,

$$c_2 = -\frac{\sin\varphi_0\sin\theta\cos\theta}{fH}$$

$$l = \frac{\delta h}{hr},\ x = r_0\cos\varphi,\ y = r_0\sin\varphi$$

Noticing that c_0, c_1, and c_2 are constants for an image, Equation 13 is a linear function, in which l, x, and y can be determined using measurements of control points. So c_0, c_1, and c_2 can be determined by selecting some control points in the image and the object space. The error equation is hence established as Equation 14:

$$V = AX - L \tag{14}$$

where

$$V = [V_1\ V_2\ \dots\ V_m]^{\mathrm{T}}$$

$$A = \begin{bmatrix} 1 & x_1 & y_1 \\ 1 & x_2 & y_2 \\ \dots & \dots & \dots \\ 1 & x_m & y_m \end{bmatrix}$$

$$X = [c_0\ c_1\ c_2]^{\mathrm{T}}$$

$$L = [l_1\ l_2 \dots l_m]^{\mathrm{T}}$$

where m is the number of control points.

The normal equation can be represented by Equation 15 according to the theory of least-squares adjustment.

$$(A^{\mathrm{T}}A)X = A^{\mathrm{T}}L. \tag{15}$$

So the solution of X can be calculated as follows:

$$X = (A^{\mathrm{T}}A)^{-1}A^{\mathrm{T}}L. \tag{16}$$

Substituting $(r\text{-}r_0)$ for δh in Equation 13, Equation 17 can be derived by rearranging Equation 13:

$$r = \frac{r_0}{1 - h(c_0 + c_1r_0\cos\varphi + c_2r_0\sin\varphi)}. \tag{17}$$

c_0, c_1, and c_2 can be calculated by Equation 16. r_0 is known after tilt displacement correction. φ can be calculated in the polar coordinate system as shown in Figure 5, and h of every lidar point is known. So r can be calculated according to Equation 17. So by this model, the corresponding pixel a of every lidar point A can be determined through the above steps.

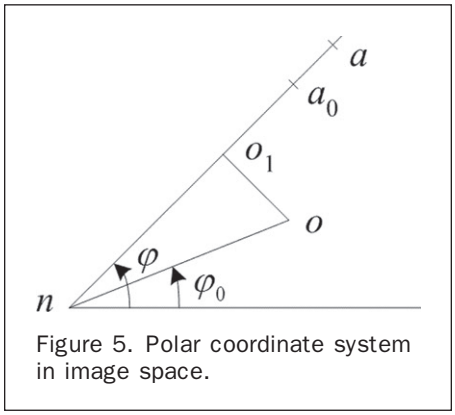

Figure 5. Polar coordinate system in image space.

Experimental Results and Discussion

In order to verify the proposed registration algorithm, experiments were conducted using the lidar data and an aerial image which cover a part of the downtown area of Jingzhou City, Hubei Province, China. The two types of data were acquired simultaneously in February 2008. The flying height was 700 m, and the lidar data was acquired by a Leica ALS50 system. The average point spacing along flying direction was 0.5 m. The average point spacing across flying direction was 0.3 m. The aerial image was captured by a RCD105 digital camera. The image resolution is 0.18 m. The image data has both IOPs and EOPs as shown in Table 1. To examine the proposed algorithm and compare it with DLT, we simply neglect these parameters. Meanwhile, we use these parameters when examining traditional photogrammetric algorithms for period comparison. The test data are shown in Plate 1.

The lidar point clouds are classified by filtering and building detection as shown in Plate 2a and 2b. The control points are selected manually in the lidar point cloud and aerial image, respectively. They are divided into two types. One type is ground points as shown in Plate 2c, which is used for Tilt Displacement Correction. Another type is object points mainly residing on roof corners as shown in Plate 2d, which are used for Height Displacement Correction.

In our study, height displacement is calculated according to the photo nadir point which is determined by intersecting perpendicular lines on the image. The perpendicular

TABLE 1. IOP AND EOP OF AERIAL IMAGE

IOP			
Principal point x (m)		Principal point y (m)	Focal length (m)
0.0000978078		−0.00016021344	−0.036099408097184
EOP			
Xs (m)	620700.900	Pitch (rad)	2.77132
Ys (m)	3354349.874	Roll (rad)	−5.72936
Zs (m)	759.153	Heading (rad)	90.41530

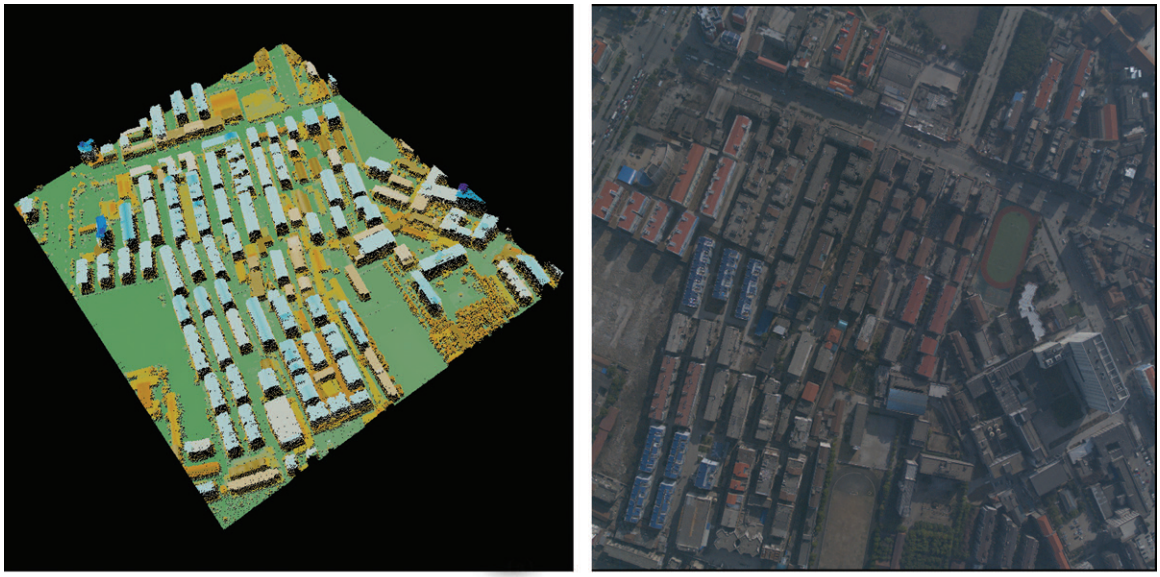

Plate 1. Test datasets: (a) lidar point clouds rendering by elevation, and (b) aerial image.

lines are straight lines fitted by the sample points along intersection lines of building walls as shown in Figure 6a. The intersection point of these perpendicular lines is obtained by least-squares adjustment as shown in Figure 6b.

In this experiment, 23 pairs of corresponding points are selected as control points for displacement correction, in which 12 pairs are for the Tilt Displacement Correction as shown in Plate 3a, and 11 pairs are for the Height Displacement Correction as shown in Plate 3b. Those control points are selected manually on the image and in the lidar point clouds, respectively.

In our experiment, the tilt displacement is corrected by the following quadratic polynomial functions:

$$x = a_0 + a_1X + a_2Y + a_3X^2 + a_4XY + a_5Y^2$$
$$y = b_0 + b_1X + b_2Y + b_3X^2 + b_4XY + b_5Y^2. \quad (18)$$

The corresponding relation of lidar points and pixels recreated after the Tilt Displacement Correction is shown as Plate 4a, where every lidar point is displayed using the color of its corresponding pixel. It shows that the lidar point clouds and the aerial image are nearly registered except for the height displacements. Some pixels on roofs appear on ground lidar points. After both tilt and height displacement are corrected, the correspondent relation of lidar point clouds and image pixels is shown as Plate 4b. Plate 5 is a detailed image of the registration results. The plates show that, with the tilt and height displacement correction working together, the final registration is visually accurate. The following quantitative assessment further reveals this.

Tables 2 and 3 present the quantitative assessment of the proposed registration algorithm. Table 2 shows the errors of the 12 ground control points for Tilt Displacement Correction before height displacement is corrected. After both the tilt and height displacement are corrected, the errors of the 11 object control points of Height Displacement Correction are shown in Table 3.

In order to compare the proposed algorithm with the traditional photogrammetric algorithm, the lidar point clouds and aerial image were also registered by (a) the space resection algorithm based on the collinearity equations, and (b) Direct Linear Transform (DLT), using the above 23 control points. After iterative calculation, the EOPs deduced from space resection are shown in Table 4. Table 5 presents a quantitative comparison of the three registration algorithms. It shows that the proposed

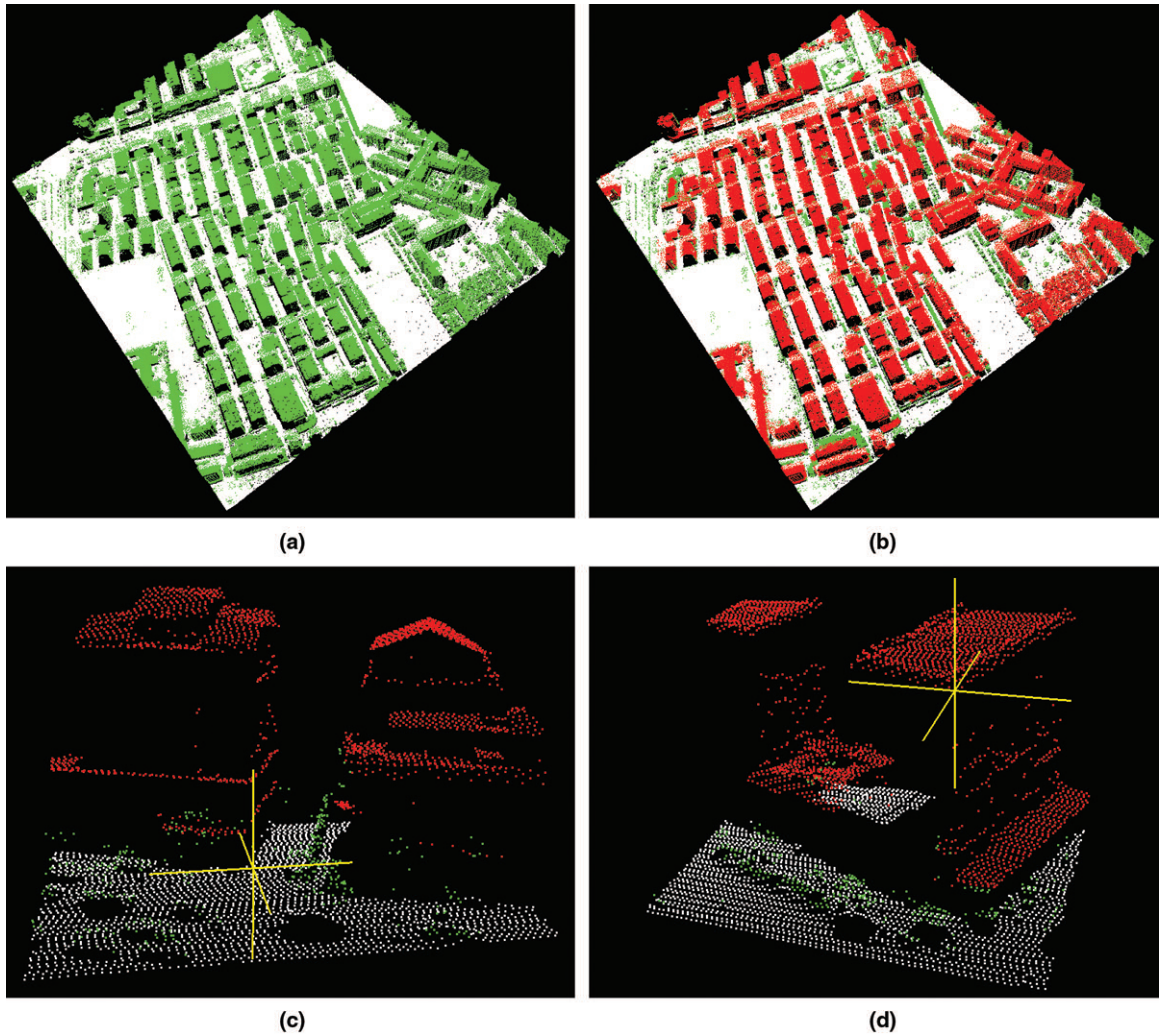

Plate 2. Selecting control points in lidar point clouds: (a) Result after filtering, (b) Result after building detection, (c) Selecting control points from ground points for Tilt Displacement Correction, and (d) Selecting control points from object points for Height Displacement Correction (red: building points, green: aboveground non-building points, white: ground points, yellow: control point).

algorithm achieves the same or even a slightly better accuracy level than that of the space resection algorithm, and is far better than DLT.

Conclusions

In this paper, we have presented a novel registration algorithm, Two-step Displacement Correction, for lidar point clouds and an aerial image without orientation parameters. The proposed algorithm is a combination of two sequential displacement corrections, i.e., Tilt Displacement Correction and Height Displacement Correction. The algorithm is demonstrated as feasible and efficient to accurately register aerial image to lidar point clouds, specifically when the orientation parameters of the image are not available. The following statements can be concluded:

1. The algorithm can accurately register the aerial images without orientation parameters and achieve the same accuracy level of the traditional photogrammetric space resection algorithm.
2. The model of the Height Displacement Correction is based on rigorous geometric functions. It is able to accurately fit height displacement of any imaging angle. It builds a linear bridge between object space and image space, and the two spaces can have different units. Pixel coordinate system can be directly used in the registration process.
3. The whole registration procedure does not need any orientation parameters of the image as either known parameter or initial values for iteration. This makes it possible that the aerial images acquired by non-metric cameras or other ways can be used for the fusion with lidar point clouds.
4. All equations used in the proposed Height Displacement Correction algorithm are linear, so the solution is computation-efficient compared with the iteration calculation of the traditional nonlinear algorithms.
5. The proposed algorithm is based on a rigorous model, in which the original coefficients have physical meaning. These coefficients are different from the space resection model.

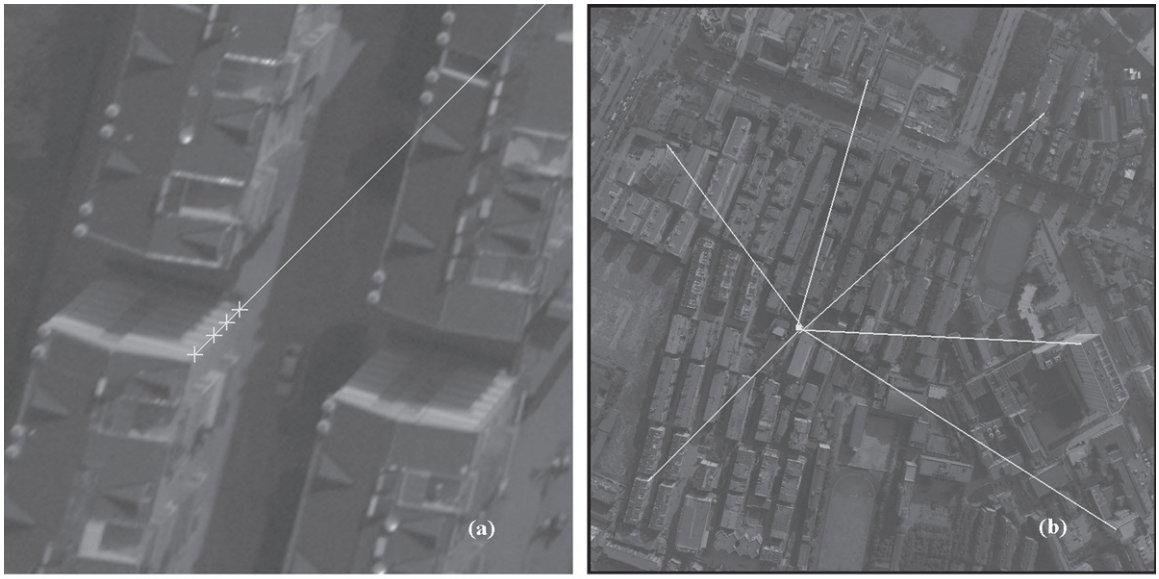

(a) (b)

Figure 6. Determination of the photo nadir point using perpendicular lines: (a) Fitting a perpendicular line on the image, and (b) The photo nadir point calculated by intersecting perpendicular lines.

(a) (b)

Plate 3. Distribution of the control points on the image: (a) The control points for Tilt Displacement Correction, and (b) The control points for Height Displacement Correction (Yellow crosses are control points).

Some of these parameters only play intermediate roles and are not resolved.

6. The proposed algorithm is also different from those generalized sensor models such as RFM or DLT, though all of them do not depend on orientation parameters. The coefficients in these generalized sensor models do not have physical meanings, while the original parameters in the proposed algorithm are physically meaningful.

However, the proposed algorithm also requires some prerequisites. Ground control points are necessary for Tilt Displacements Correction. These control points are required to

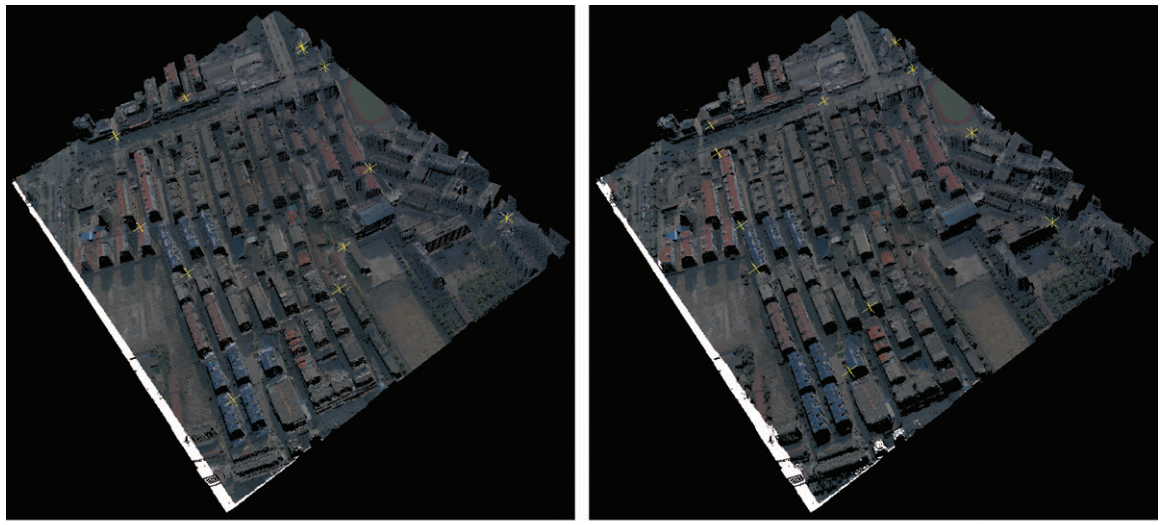

(a) (b)

Plate 4. Perspective projection of lidar points in the color of their corresponding pixels. (a) Overview after Tilt Displacement Correction, and (b) Overview after both Tilt and Height Displacement Correction (Yellow cross are control points).

avoid large height differences. Also, this algorithm relies on the photo nadir point which is collected by intersection of expenditure lines. Though these expenditure lines are easily collected in urban areas from building's corner lines, this partially limits the possible applications of the proposed algorithm.

Acknowledgments

This study was supported by the 973 Program (2006CB701304), the 863 Program (2007AA12Z217), the National Natural Science Foundation of China (40721001), and the Program for New Century Excellent Talents in University (NCET-06-0619). Steve McClure assisted with language editing.

References

Abedini, A., M. Hahn, and F. Samadzadegan, 2008. An investigation into the registration of LiDAR intensity data and aerial images using the SIFT approach, *International Archives of Photogrammetry, Remote Sensing and Spatial Information Sciences*, 37(B1):169–175

Brenner, C., 2005. Building reconstruction from images and laser scanning, *International Journal of Applied Earth Observation and Geoinformation*, 6(3–4):187–198.

Chen, L.-C., T.-A. Teo, C.-H. Hsieh, and J.-Y. Rau, 2006. Reconstruction of building models with curvilinear boundaries from laser scanner and aerial imagery, *Advances in Image and Video Technology*, LNCS, Springer, Berlin, Vol. 4319, pp. 24–33.

Dalponte, M., L. Bruzzone, and D. Gianelle, 2008. Fusion of hyperspectral and LiDAR remote sensing data for classification of complex forest areas, *IEEE Transactions on Geoscience and Remote Sensing*, 46(5):1416–1427.

Delara, R., Jr., E.A. Mitishita, and A. Habib, 2004. Bundle adjustment of images from non-metric CCD camera using LiDAR data as control points, *International Archives of Photogrammetry, Remote Sensing and Spatial Information Sciences*, 35(B3):13–18.

Demir, N., D. Poli, and E. Baltsavias, 2008. Extraction of buildings and trees using images and LiDAR data, *International Archives of Photogrammetry, Remote Sensing and Spatial Information Sciences*, 37:313–318.

Deng, F., M. Hu, and H. Guan, 2008. Automatic registration between LiDAR and digital images, *International Archives of Photogrammetry, Remote Sensing and Spatial Information Sciences*, 37(B1):487–490

Dorninger, P., and N. Pfeifer, 2008. A comprehensive automated 3D approach for building extraction, reconstruction, and regularization from airborne laser scanning point clouds, *Sensors*, 8(11):7323–7343.

Fujii, K., and T. Arikawa, 2002, Urban object reconstruction using airborne laser elevation image and aerial image, *IEEE Transactions on Geoscience and Remote Sensing*, 40(10):2234–2240.

Habib, A., M.S. Ghanma, E.A. Mitishita, E.M. Kim, and C.J. Kim, 2005a. Image georeferencing using LiDAR data, *Proceedings of IGARSS'05*, Seoul, South Korea, Vol. 2, pp.1158–1161.

Habib, A., M. Ghanma, M. Morgan, and R. Al-Ruzouq, 2005b. Photogrammetric and LiDAR data registration using linear features, *Photogrammetric Engineering & Remote Sensing*, 71(6):699–707.

Habib, A., S. Shin, C. Kim, and M. Al-Durgham, 2006. Integration of photogrammetric and LiDAR data in a multi-primitive triangulation environment, *Innovations in 3D Geo Information Systems*, Springer, Berlin, Part 2, pp.29–45.

Hu, J., S. You, and U. Neumann, 2006. Integrating LiDAR, aerial image and ground images for complete urban building modeling, *Proceedings of 3DPVT '06*, pp. 184–191.

Jiang, G., T. Jiang, Y. Wang, and H. Gong, 2007. Space resection independent of initial value based on unit quaternions, *Acta Geodaetica et Cartographica Sinica*, 36(2):169–175.

Li, Y., and H. Wu, 2008a. Filtering airborne LiDAR data based on morphological gradient, *Journal of Remote Sensing*, 12(4):633–639.

Li, Y., and H. Wu, 2008b. Adaptive building edge detection by combining LiDAR data and aerial images, *International Archives of Photogrammetry, Remote Sensing and Spatial Information Sciences*, 37(B1), pp.197–202.

Liu, X., Z. Zhang, J. Peterson and S. Chandra, 2007. LiDAR-derived high quality ground control information and DEM for image orthorectification, *GeoInformatica*, 11(1):37–53.

McIntosh, K., and A. Krupnik, 2002. Integration of laser-derived DSMs and matched image edges for generating an accurate

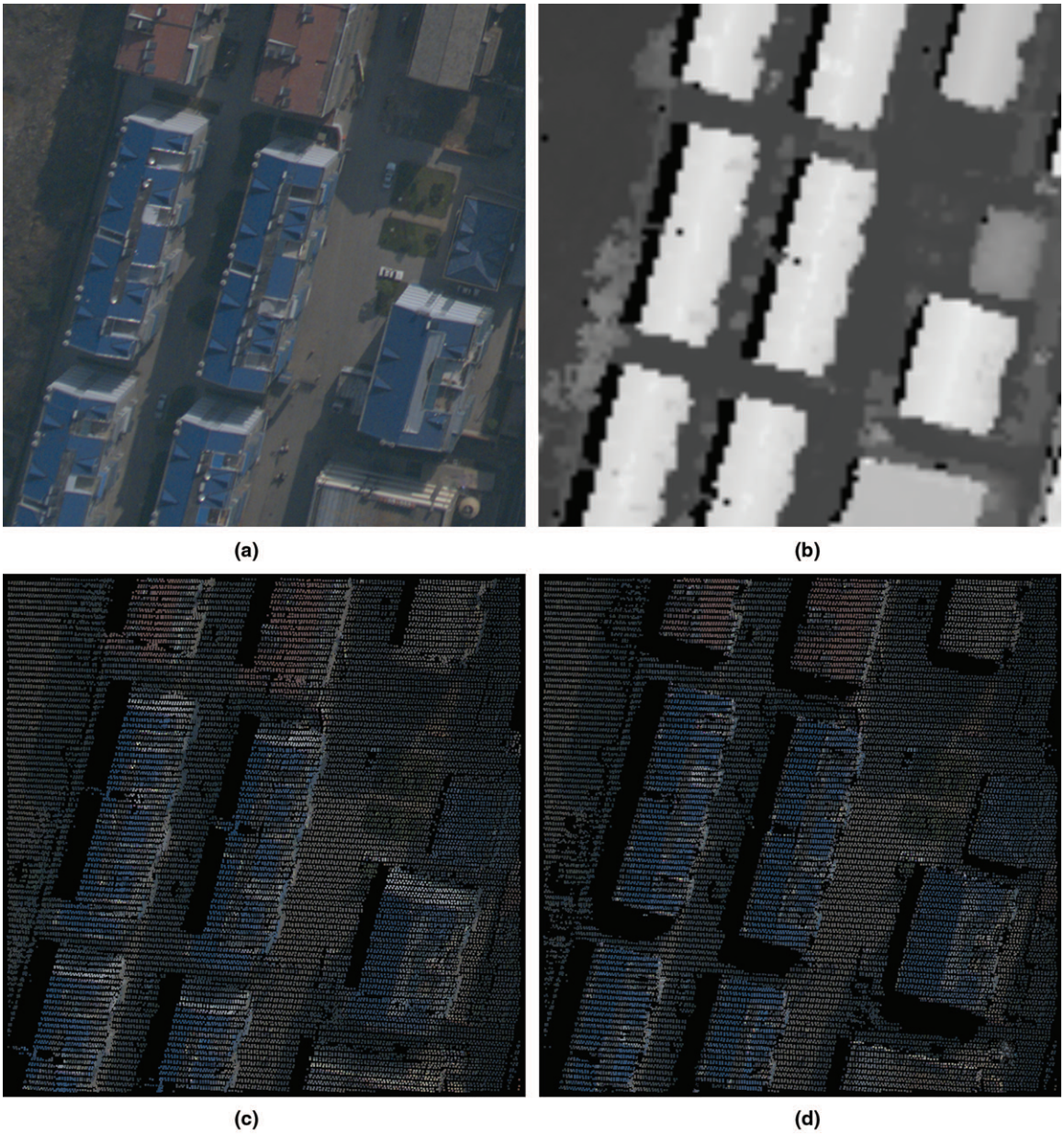

Plate 5. Detailed Image of the registration results of the proposed algorithm: (a) Aerial image, (b) Depth image generated from lidar point clouds, (c) Orthographic projection of lidar points in the color of their corresponding pixels after Tilt Displacement Correction, and (d) Orthographic projection of lidar points in the color of their corresponding pixels after both tilt and Height Displacement Correction.

surface model, *ISPRS Journal of Photogrammetry and Remote Sensing*, 56(3):167–176.

Murakami, H., K. Nakagawa, H. Hasegawa, T. Shibata, and E. Iwanami, 1999. Change detection of buildings using an airborne laser scanner, *ISPRS Journal of Photogrammetry and Remote Sensing*, 54(2–3):148–152.

Poullis, C., and S. You, 2009. Photorealistic large-scale urban city model reconstruction, *IEEE Transactions on Visualization and Computer Graphics*, 15(3):1–15.

Rottensteiner, F., and J. Jansa, 2002. Automatic extraction of buildings from LiDAR data and aerial images, *International Archives of Photogrammetry, Remote Sensing and Spatial Information Sciences*, 34(4):295–301.

Rottensteiner, F., 2003. Automatic generation of high-quality building models from LiDAR data, *IEEE Computer Graphics and Applications*, 23(6):42–50.

Rottensteiner, F., J. Trinder, S. Clode, and K. Kubik, 2005. Using the Dempster-Shafer method for the fusion of LiDAR data and multi-spectral images for building detection, *Information Fusion*, 6(4):283–300.

Secord, J., and A. Zakhor, 2007. Tree detection in urban regions using aerial LiDAR and image data, *IEEE Geoscience and Remote Sensing Letters*, 4(2):196–200.

Tao, C.V., and Y. Hu, 2001, Use of the rational function model for image rectification, *Canadian Journal of Remote Sensing*, 17(6):593–602.

Table 2. The errors of the 12 Ground Control Points after Tilt Displacement Corrected

Control point	*x* (pixel)	*y* (pixel)	Height (m)
1	−3	3	5.03
2	0	−6	5.50
3	5	6	6.08
4	1	−1	5.70
5	−7	−6	5.71
6	−4	0	5.98
7	0	2	6.08
8	0	0	6.20
9	−3	−2	6.04
10	5	1	6.04
11	−1	−2	5.29
12	1	−1	6.48
RMSE	3.36	3.31	

Table 3. The Errors of the 11 Object Control Points after Both Tilt and Height Displacement Corrected

Control point	*x* (pixel)	*y* (pixel)	Height (m)
1	−4	3	20.37
2	6	7	22.84
3	−4	4	27.86
4	2	3	29.44
5	4	−2	30.43
6	−1	−5	28.38
7	−2	−3	27.99
8	0	−6	27.77
9	0	0	26.46
10	1	−3	31.96
11	−2	−8	29.55
RMSE	2.98	4.57	

Table 4. EOP Calculated by Space Resection based on Collinear Equations

	Before registration	After registration
Xs (m)	620700.90	620701.82
Ys (m)	3354349.87	3354349.32
Zs (m)	759.15	765.64
Pitch (rad)	2.77	3.18
Roll (rad)	−5.72	−3.04
Heading (rad)	90.41	92.67

You, H., and S. Zhang, 2006. 3D building reconstruction from aerial CCD image and sparse laser sample data, *Optics and Lasers in Engineering*, 44(6):555–566.

Zhang, J., Y. Zhang, and F. Fang, 2007. Absolute orientation of aerial imagery over urban areas combined with vertical lines, *Geomatics and Information Science of Wuhan University*, 32(3):197–200.

Zhang, Z. and J. Zhang, 2004. Generalized point photogrammetry and its application, *International Archives of Photogrammetry, Remote Sensing and Spatial Information Sciences*, 35(B2):77–81.

Zhang, Z. and Y. Zhang, 2007. Study of the vertical lines supported aerial triangulation over urban areas, Geomatics and Information Science of Wuhan, 32(8):659–662.

Zhang, Z., Y. Zhang, J. Zhang, and H. Zhang, 2008. Photogrammetric modeling of linear features with generalized point photogrammetry, *Photogrammetric Engineering & Remote Sensing*, 74(9):1119–1127.

Zhou, G., C. Song, J. Simmers, and P. Cheng, 2004. Urban 3D GIS from LiDAR and digital aerial images, *Computers & Geosciences*, 30(4):345–353.

(Received 14 July 2009; accepted 04 November 2009; final version 28 January 2010)

Table 5. The Error Comparison of the Control Points using Different Registration Algorithms

	Our algorithm		Space resection		DLT		
Control point	*x* (pixel)	*y* (pixel)	*x* (pixel)	*y* (pixel)	*x* (pixel)	*y* (pixel)	Height (m)
1	−2	1	−2	3	−19	70	5.03
2	0	−6	0	−2	9	60	5.50
3	6	7	6	5	52	54	6.08
4	1	−1	1	−3	49	48	5.70
5	−7	−5	−6	−7	41	31	5.71
6	−3	0	−2	2	31	1	5.98
7	1	2	1	7	14	−10	6.08
8	0	0	0	4	4	−22	6.20
9	−3	−1	−5	−5	−42	−41	6.04
10	6	1	7	4	−19	9	6.04
11	0	−2	1	0	−28	29	5.29
12	3	−2	2	−8	48	−44	6.48
13	−4	3	−5	1	−9	27	20.37
14	6	7	3	3	19	18	22.84
15	−4	4	−6	3	−1	4	27.86
16	2	3	0	1	1	1	29.44
17	4	−2	3	3	3	4	30.43
18	−1	−5	−3	−4	−4	−6	28.38
19	−2	−3	0	−1	−2	−1	27.99
20	0	−6	1	−4	−1	−2	27.77
21	0	0	0	−1	−2	7	26.46
22	1	−3	−3	−5	−5	−7	31.96
23	−2	−8	−5	−6	−4	−5	29.55
RMSE	3.31	3.93	3.51	4.13	24.78	30.25	

Forthcoming Articles

Francis P. Padula and *John R. Schott*, Historic Calibration of the Thermal Infrared Band of Landsat-5 TM.

Hasi Bagan and *Yoshiki Yamagata*, Improved Subspace Classification Method for Multispectral Remote Sensing Image Classification.

Keith T. Weber and *Fang Chen*, Detection Thresholds for Rare, Spectrally Unique Targets within Semiarid Rangelands.

Jan Stuckens, *Ben Somers*, *Gene L. Albtigo*, *Sebinasi Dzikiti*, *Willem W. Verstraeten*, *Rony Swennen*, *Stephan Verreyne*, and *Pol Coppin*, Off-nadir Viewing for Reducing Spectral Mixing Issues in Citrus Orchards.

Meng Bian, *Andrew K. Skidmore*, *Martin Schlerf*, *Teng Fei*, *Yanfang Liu*, and *Tiejun Wang*, Reflectance Spectroscopy of Biochemical Components as Indicators of Tea (*Camellia Sinensis*) Quality.

A. Cuartero, *A.M. Felicísimo*, *M.E. Polo*, *A. Caro*, and *P.G. Rodríguez*, Positional Accuracy Analysis of Satellite Imagery by Circular Statistics.

Liang Cheng, *Jianya Gong*, *Manchun Li*, and *Younxue Liu*, 3D Building Model Reconstruction from Mulit-view Aerial Imagery and Lidar Data.

Rama Prasada Mohapatra and *Changshan Wu*, High Resolution Impervious Surface Estimation: An Integration of Ikonos and Landsat-7 ETM+ Imagery.

Tiejun Wang, Andrew K. Skidmore, Zhigao Zeng, Pieter S.A. Beck, Yali Si, Yanling Song, Xuehua Liu, and Herbert H.T. Prins, Migration Patterns if Two Endangered Sympatric Species from a Remote Sensing Perspective.

Jaehong Oh, *Won Hee Lee*, *Charles K. Toth*, *Dorota A. Grejner-Brzezinska*, and *Changno Lee*, A Piecewise Approach to Epipolar Resampling of Pushbroom Satellite Images Based on RCP.

Frank Crosby, *Haomin Zhou*, and *Quyen Huynh*, Total Variation Methods for Three Dimensional Lidar Image Denoising.

Stefan Auer, *Timo Balz*, *Susanne Becker*, and *Richard Bamler*, 3D SAR Simulation of Urban Areas Based on Detailed Building Models.

Xiaojun Yang, Parameterizing Support Vector Machines for Land Cover Classification.

Amy C. Burnicki, Modeling the Probability of Misclassification on a Map of Land Cover Change.

Minho Kim, *James B. Holt*, and *Marguerite Madden*, Comparison of Global- and Local-scale Pansharpening for Rapid Assessment of Humanitarian Emergencies.

Ji Zhu, *Jiancheng Shi*, *Hanfang Chu*, *Jiawen Hu*, *Xiaozhou Li*, and *Wei Li*, Remote Sensing Classification Using Fractal Dimensions over a Subtropical Hilly Region.